Fast-timing measurements in the ground-state band of ^{114}Pd

E. R. Gamba,[1] A. M. Bruce,[1,*] S. Lalkovski,[2,†] M. Rudigier,[2] S. Bottoni,[3,‡] M. P. Carpenter,[3] S. Zhu,[3] J. T. Anderson,[3] A. D. Ayangeakaa,[3,§] T. A. Berry,[2] I. Burrows,[4] M. Carmona Gallardo,[5] R. J. Carroll,[2] P. Copp,[6] D. M. Cullen,[7] T. Daniel,[2,¶] G. Fernández Martínez,[8] J. P. Greene,[3] L. A. Gurgi,[2] D. J. Hartley,[9] R. Ilieva,[2] S. Ilieva,[8] F. G. Kondev,[10] T. Kröll,[8] G. J. Lane,[11] T. Lauritsen,[3] I. Lazarus,[4] G. Lotay,[2] C. R. Niţă,[12] Zs. Podolyák,[2] V. Pucknell,[4] M. Reed,[11] P. H. Regan,[2,13] J. Rohrer,[3] J. Sethi,[3] D. Seweryniak,[3] C. M. Shand,[2] J. Simpson,[4] M. Smoleń,[14] E. A. Stefanova,[15] V. Vedia,[5] and O. Yordanov[15]

[1]*School of Computing, Engineering and Mathematics, University of Brighton, Brighton BN2 4GJ, United Kingdom*
[2]*Department of Physics, University of Surrey, Guildford GU2 7XH, United Kingdom*
[3]*Physics Division, Argonne National Laboratory, Argonne, Illinois 60439, USA*
[4]*STFC Daresbury Laboratory, Daresbury, Warrington WA4 4AD, United Kingdom*
[5]*Grupo de Física Nuclear, Universidad Complutense, CEI Moncloa, ES-28040 Madrid, Spain*
[6]*Department of Physics and Applied Physics, University of Massachusetts Lowell, Lowell, Massachusetts 01854, USA*
[7]*School of Physics and Astronomy, University of Manchester, Manchester M13 9PL, United Kingdom*
[8]*Institut für Kernphysik, TU Darmstadt, Schlossgartenstrasse 9, 64289 Darmstadt, Germany*
[9]*Department of Physics, U.S. Naval Academy, Annapolis, Maryland 21402, USA*
[10]*Nuclear Engineering Division, Argonne National Laboratory, Argonne, Illinois 60439, USA*
[11]*Department of Nuclear Physics, R.S.P.E., Australian National University, Canberra 0200, Australia*
[12]*Horia Hulubei National Institute of Physics and Nuclear Engineering, Bucharest-Măgurele, Romania*
[13]*AIR Division, NPL, Teddington TW11 0LW, United Kingdom*
[14]*School of Engineering and Science, University of the West of Scotland, Paisley PA1 2BE, United Kingdom*
[15]*INRNE, Bulgarian Academy of Sciences, 1784 Sofia, Bulgaria*

(Received 29 June 2019; revised manuscript received 31 August 2019; published 11 October 2019)

Using a hybrid Gammasphere array coupled to 25 $LaBr_3$(Ce) detectors, the lifetimes of the first three levels of the yrast band in ^{114}Pd, populated via ^{252}Cf decay, have been measured. The measured lifetimes are $\tau_{2^+} = 103(10)$ ps, $\tau_{4^+} = 22(13)$ ps, and $\tau_{6^+} \leqslant 10$ ps for the 2_1^+, 4_1^+, and 6_1^+ levels, respectively. Palladium-114 was predicted to be the most deformed isotope of its isotopic chain, and spectroscopic studies have suggested it might also be a candidate nucleus for low-spin stable triaxiality. From the lifetimes measured in this work, reduced transition probabilities $B(E2; J \to J-2)$ are calculated and compared with interacting boson model, projected shell model, and collective model calculations from the literature. The experimental ratio $R_{B(E2)} = B(E2; 4_1^+ \to 2_1^+)/B(E2; 2_1^+ \to 0_1^+) = 0.80(42)$ is measured for the first time in ^{114}Pd and compared with the known values $R_{B(E2)}$ in the palladium isotopic chain: the systematics suggest that, for $N = 68$, a transition from γ-unstable to a more rigid γ-deformed nuclear shape occurs.

DOI: 10.1103/PhysRevC.100.044309

I. INTRODUCTION

Nuclear lifetimes are very important physical observables that are able to provide fundamental information on the structure of the atomic nucleus. The lifetime of a nuclear excited level can be related to the quadrupole reduced transition probability $B(E2; J \to J-2)$ of the level, which is in turn related to the intrinsic quadrupole moment Q_0. This is strictly dependent on the quadrupole deformation parameter β_2 [1]. By measuring the lifetime of nuclear excited levels it is therefore possible to quantify the occurrence of deformation across the nuclear chart as a function of proton and neutron numbers. Nuclear deformation has been studied systematically in regions far from shell closures, such as $A \simeq 110$, $A \simeq 150$, and $A \simeq 250$, where nuclei are known to be characterized by nonspherical shapes [2]. Together with oblate ($\beta_2 < 0$) and prolate ($\beta_2 > 0$) deformed nuclei, a third possibility is represented by cases of static or dynamical triaxial deformation ($\gamma \neq n\frac{\pi}{3}$), where all three nuclear axes have different lengths. Indications of triaxial deformation have been observed in the molybdenum ($Z = 42$) [3,4], ruthenium ($Z = 44$) [5–7], and palladium ($Z = 46$) [8] isotopic chains.

*Alison.Bruce@brighton.ac.uk
†Present address: Department of Nuclear Engineering, Faculty of Physics, University of Sofia "St. Kl. Ohridski", Sofia 1164, Bulgaria.
‡Present address: Dipartimento di Fisica, Università degli Studi di Milano and INFN, 20133 Milano, Italy.
§Present address: Department of Physics, U.S. Naval Academy, Annapolis, Maryland 21402, USA.
¶Present address: Department of Physics, Benue State University, P.M.B., 102119 Makurdi, Nigeria.

The palladium isotopic chain lies between Cd ($Z = 48$), usually treated as vibrational [9], and Ru ($Z = 44$) showing γ-soft and rigid-triaxial rotor behavior [5,6].

Studies have indicated the vibrational behavior of ^{106,108}Pd isotopes [10], which approaches that of a γ-soft rotor for $A \leqslant 110$ [8]. Spectroscopic investigations of higher mass $^{116-120}$Pd isotopes [11–13] suggest that, as the neutron number increases, the behavior of Pd isotopes moves back to that of an anharmonic vibrator showing a loss of collectivity [14].

The isotope ^{114}Pd ($N = 68$) lies very close to the mid shell at $N = 66$, between the $N = 50$ and $N = 82$ neutron shell closures, and it was shown in Ref. [15] that the maximum of rotational collectivity is reached for this isotope. Furthermore, for $N = 68$, the maximum value of the ratio $E(4_1^+)/E(2_1^+) \simeq 2.6$ is reached [15]. Similarly to the case of the ruthenium isotopic chain, this never reaches the rotational limit of 3.33, which is expected for axially symmetric nuclei.

From a spectroscopic perspective, for the isotope ^{114}Pd, the energy spacing of the yrast band follows quite remarkably the $\sim J(J+6)$ pattern expected for both the Wilets-Jean γ-soft model [16] and the Davydov-Filippov rigid triaxial rotor model [17]. Two important signatures of triaxial deformation are the $E_{2_2^+}/E_{4_1^+}$ and $E_{2_2^+}/E_{2_1^+}$ ratios which, for this case, are 0.8 and 2.1, respectively. The former is reported by both the Wilets-Jean and Davydov-Filippov models to be a signature of strong departure from axiality, while the latter is consistent with a γ deformation parameter of 27.5°.

A distinction between γ-soft and rigid triaxial behavior can be established when looking at the energy spacing between levels inside the quasi-γ band [18]. In Ref. [19] Pd isotopes were systematically analyzed in terms of the *staggering parameter* $S(J)$, defined as

$$S(J) = \frac{[E(J) - 2E(J-1) + E(J-2)]}{E(2_1^+)}, \qquad (1)$$

where $E(J)$ is the energy of a level with spin J in the quasi-γ band. In the case of γ-soft nuclei, the $S(J)$ parameter is expected to take positive values for the odd-spin levels and negative values for the even-spin ones, while the opposite is true for the γ-rigid case [20]. Figure 1 shows the behavior of the parameter $S(J)$ for the quasi-γ band in the nuclei $^{108-118}$Pd. An inversion of the type of triaxiality, from γ-soft to that of a rigid rotor, is observed for ^{114}Pd.

In this work, ^{114}Pd nuclei were produced via the spontaneous fission of ^{252}Cf, which is able to populate the regions of deformed nuclei around mass numbers $A \simeq 110$ and $A \simeq 150$ with higher fission yields for neutron-rich nuclei with respect to other neutron-induced fission reactions [21]. The measured lifetimes of the 2_1^+, 4_1^+, and 6_1^+ levels, are used to calculate $B(E2; J \to J-2)$ transition probabilities and then compared with theoretical calculations from the literature, performed using the interacting boson model (standard and triaxial IBM-1) [22,23], the projected shell model (PSM) [24], and the collective model [2,25] with the inclusion of the Killingbeck potential [26]. Since $R_{B(E2)} = B(E2; 4_1^+ \to 2_1^+)/B(E2; 2_1^+ \to 0_1^+)$ ratios are known to be able to give information about the type of nuclear deformation, and are well established for nuclei in the mass region $A \simeq 110$, of prime interest for the present work is to obtain new information on the $R_{B(E2)}$ ratio for ^{114}Pd. Furthermore, the experimental $R_{B(E2)}$ ratio obtained for ^{114}Pd is compared with those from the neighboring even-N palladium isotopes, when these are available, and with the theoretical values predicted by the vibrational, rigid axial rotor, Davydov-Filippov, and Wilets-Jean models.

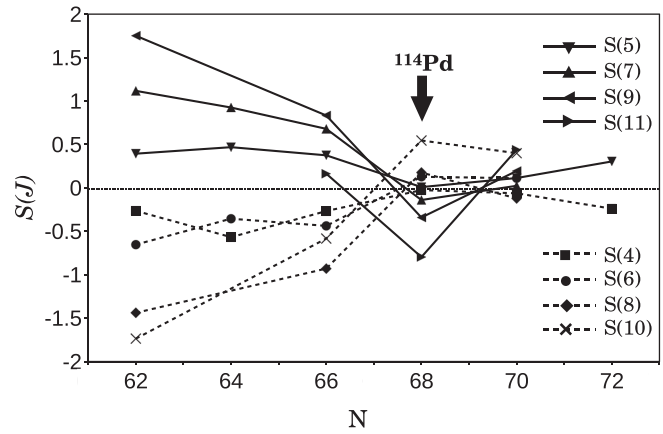

FIG. 1. Values of $S(J)$ for $^{108-118}$Pd nuclei, calculated from Eq. (1), using values taken from Ref. [27]. The staggering parameters for odd-J levels (solid lines) are compared with those for even-J levels (dashed lines). Figure adapted from Ref. [19].

II. EXPERIMENTAL SETUP

The experimental setup combined the Gammasphere [28] and FATIMA [29] arrays at the Argonne National Laboratory (USA). This was the first time that Gammasphere was coupled to such a large number of $LaBr_3$(Ce) scintillator detectors using a fully digital acquisition setup. ^{114}Pd nuclei were observed following the spontaneous fission of a 34.4 μCi ^{252}Cf source placed at the center of a 4π hybrid array made of 51 Compton-suppressed high-purity germanium (HPGe) detectors from the Gammasphere array coupled to 25 $LaBr_3$(Ce) scintillator detectors from the FATIMA array.

The source consisted of a sample of 183 ng of ^{252}Cf electrodeposited on a platinum disk of ≈1.6 cm diameter and 0.25 mm thickness with an active spot of ≈1.27 cm diameter. A second platinum disk of the same size was attached to the other side of the source using an indium layer of 250 μm/cm^2. The resulting disk sandwiched the source between the two Pt disks, therefore fission fragments were equally absorbed on both sides of the disk and no Doppler-shifted γ rays or increased line widths were observed.

Each $LaBr_3$(Ce) detector consisted of a cylindrical crystal 3.8 cm in diameter and 5.1 cm in length, coupled with a Hammamatsu H10570 photomultiplier assembly comprising a R9779 phototube. A 5-mm-thick lead layer covered the side of each $LaBr_3$(Ce) crystal in order to absorb Compton-scattered γ rays from adjacent crystals. A fully digital acquisition system (DAQ) was used on the entire $LaBr_3$(Ce) array for the first time. On the $LaBr_3$(Ce) side, events made of at least two γ rays within a time window of 200 ns were collected. Independently, fold $\geqslant$1 events were collected in the Gammasphere array. The two DAQ data streams

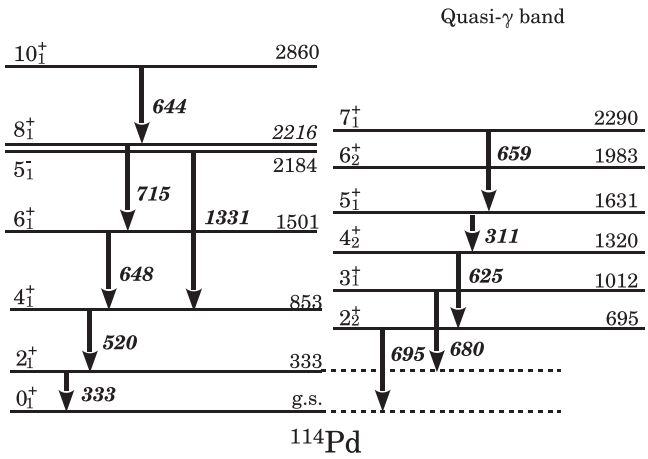

FIG. 2. Partial level scheme of ^{114}Pd, including the ground-state band and the quasi-γ band, of interest for this work. For clarity, the 5^-_1 level is also included (see text for details) [27]. All arrows have equal widths and do not reflect the γ-ray intensities.

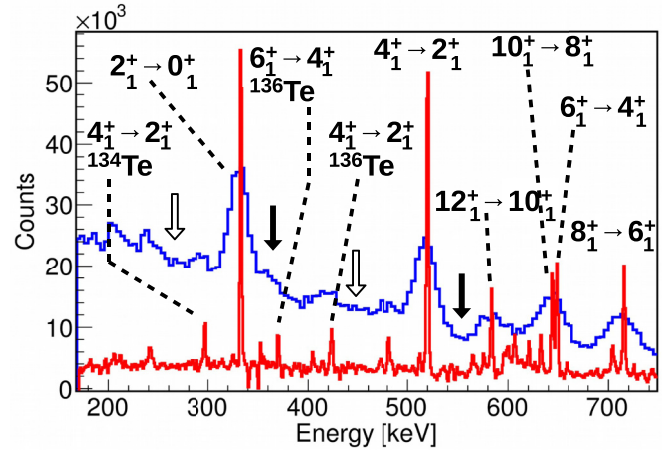

FIG. 3. Gammasphere (red) and $LaBr_3$(Ce) (blue) energy spectra, obtained by adding together four FEP(HPGe)-gated energy spectra and by subtracting four background-gated energy spectra; see text for details. The $4^+_1 \rightarrow 2^+_1$ and $2^+_1 \rightarrow 0^+_{g.s.}$ transitions in ^{114}Pd are clearly visible. One can also notice the large number of (small) transitions, produced by ^{114}Pd itself and the fission partners ^{134,136}Te. For the purpose of this measurement these small peaks are considered as contaminants. The four arrows indicate the left (unfilled) and right (filled) background regions considered for the timing background subtraction (see text and Fig. 4).

were eventually merged using a coincidence time window of 500 ns between the fold $\geqslant$2 $LaBr_3$(Ce) and fold $\geqslant$1 HPGe events, in order to give events of the type $\gamma(LaBr_3(Ce))$-$\gamma(LaBr_3(Ce))$-γ(HPGe). During a 30-day-long run a total of 2.6×10^9 E_γ(HPGe)-$E_\gamma(LaBr_3(Ce))$-$E_\gamma(LaBr_3(Ce))$ events were collected. For a detailed description of the acquisition system see Ref. [30].

III. DATA ANALYSIS AND RESULTS

The level of statistics obtained in this experiment only allowed the lifetimes of the 2^+_1, 4^+_1, and 6^+_1 levels in ^{114}Pd to be measured. In order to measure the three lifetimes, both $LaBr_3$(Ce) and HPGe detectors were used. Due to the superior energy resolution of HPGe detectors, E_γ(HPGe) transitions were used to select the nucleus of interest and the corresponding excited band, while cerium-doped lanthanum bromide [$LaBr_3$(Ce)] scintillator detectors, capable of accessing the subnanosecond range, were used to measure the lifetimes of interest. The large number of contaminant γ-ray peaks from the large number of fission fragments means that particular care had to be taken when applying the E_γ(HPGe) gates and when performing the lifetime measurements with the $LaBr_3$(Ce) detectors. The lifetimes measured in this work were around 100 ps or shorter, therefore the *generalized centroid difference* (GCD) method [31] was used. The background correction applied on the time information followed the *three samples* approach described in Ref. [32].

The analysis performed for the three levels used similar procedures; however, for each case, individual adjustments had to be considered. For the discussions in this section, the reader should refer to the partial level scheme of ^{114}Pd, presented in Fig. 2, where only the levels and transitions of interest for this work are presented.

A. 2^+_1 level in ^{114}Pd

For the lifetime measurement of the 2^+_1 level in ^{114}Pd, E_γ(HPGe) gates were applied on the $6^+_1 \rightarrow 4^+_1$ (648 keV), $8^+_1 \rightarrow 6^+_1$ (715 keV), $10^+_1 \rightarrow 8^+_1$ (644 keV), and $5^-_1 \rightarrow 4^+_1$ (1332 keV) transitions. For each of these full-energy-peak (FEP) gates a E_γ(HPGe) background gate was also identified. Each of these background gates was taken as close as possible to the corresponding FEP gate and the same gate width (usually 2 or 3 keV) was used. Due to the large number of peaks in the ^{252}Cf fission spectrum the selection of E_γ(HPGe) background gates required extreme care, to make sure that no peak with small amplitude was included in the background gate. The E_γ(HPGe) (red) and $E_\gamma(LaBr_3(Ce))$ (blue) energy spectra shown in Fig. 3 were obtained by adding together the four different FEP-gated energy spectra and by subtracting the four background-gated spectra, for both arrays, respectively. In both spectra the $4^+_1 \rightarrow 2^+_1$ (feeding transition at 520 keV) and $2^+_1 \rightarrow 0^+_{g.s.}$ (decay transition at 333 keV) are clearly visible, together with other higher-energy transitions from the same nucleus or its fission partners. The same FEP and background E_γ(HPGe) gates were then applied to produce eight $E_\gamma(LaBr_3(Ce))$-$E_\gamma(LaBr_3(Ce))$-ΔT cubes with coincident events. This set of eight cubes was then used to produce the final $E_\gamma(LaBr_3(Ce))$-$E_\gamma(LaBr_3(Ce))$-ΔT cube by adding together the four cubes obtained from the FEP gates and subtracting those from the background gates.

The final E_γ-E_γ-ΔT cube produced following this procedure is a so-called start-and-stop cube, i.e., the two energy axes x and y represent the energy values measured for the γ rays defining the start and stop of the measured ΔT value, respectively. Here, ΔT is defined as

$$\Delta T = T_{E_y} - T_{E_x}. \quad (2)$$

The information from the detector with the smaller identification number was put on the x axis and the other one

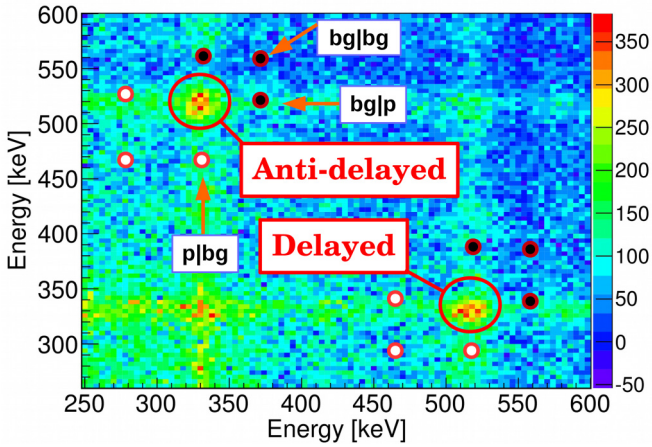

FIG. 4. Two-dimensional projection of the start and stop E_γ(LaBr$_3$(Ce))-E_γ(LaBr$_3$(Ce))-ΔT cube obtained by gating on the $6_1^+ \rightarrow 4_1^+$, $8_1^+ \rightarrow 6_1^+$, $10_1^+ \rightarrow 8_1^+$, and $5_1^- \rightarrow 4_1^+$ transitions, in ^{114}Pd, in Gammasphere. The two regions encircled by the red solid lines represent the coincidence peaks for the $4_1^+ \rightarrow 2_1^+ \rightarrow 0_{g.s.}^+$ cascade. The dots encircled in red are used to indicate the left (white) and right (black) gates applied to obtain the three background components, for both the delayed and anti-delayed time distributions. These correspond to the four arrows shown in Fig. 3.

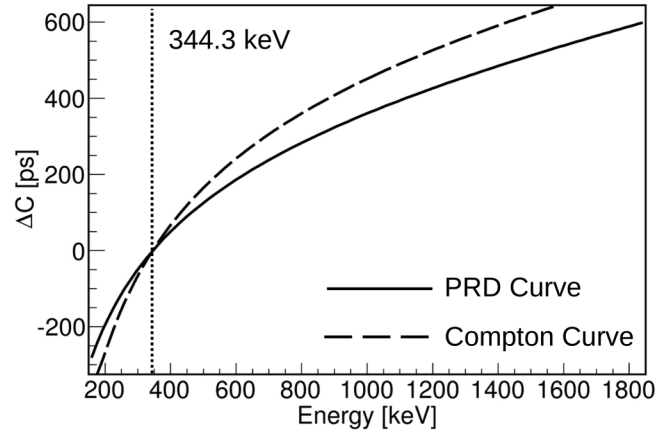

FIG. 5. Experimental PRD (solid line) and Compton (dashed line) curves, plotted using 344.3 keV as the reference energy. These are used to correct for the effect of the time walk on the position of the centroids of the FEP ($p|p$) and background ($p|bg$, $bg|p$ and $bg|bg$) time distributions, respectively. See Refs. [31,32] for a complete description of the properties of these two curves.

on the y axis. This avoids the cube being filled twice and also makes it not symmetrical. The E_γ-E_γ matrix obtained by projecting the cube on the x-y plane, for the case of the 2_1^+ level in ^{114}Pd, is shown in Fig. 4. The two coincidence peaks encircled in red contain independent events from the $4_1^+ \rightarrow 2_1^+ \rightarrow 0_{g.s.}^+$ cascade and, by gating on them, the $p|p$ (FEP-FEP) delayed and antidelayed time distributions are obtained. In order to background correct the value of the centroid position $C^m_{p|p}$ (where the label m stands for *measured*) of the delayed and antidelayed time distributions, the *three samples* approach explained in Ref. [32] was used. The *interpolation* approach was avoided due to the large number of contaminant peaks. The three samples of the $p|bg$ (FEP-background), $bg|p$ (background-FEP), and $bg|bg$ (background-background) background components were obtained from the average between the left and right gates, indicated by the white and black dots in Fig. 4, respectively. The same gates were represented in Fig. 3 by the unfilled and filled arrows.

Twelve two-dimensional background gates were considered (six for each coincidence peak) in total. For example, events showing a coincidence between the $2_1^+ \rightarrow 0_{g.s.}^+$ transition and the background gate to the right (left) of the $2_1^+ \rightarrow 0_{g.s.}^+$ transition give the right (left) gate of the $p|bg$ background component. The opposite is true for the left and right background gates of the $bg|p$ component. The two-dimensional right (left) $bg|bg$ gates, shown in Fig. 4, are obtained by combining the energies of two right (left) background gates shown in Fig. 3. From these six time distributions, three background time distributions were obtained from the weighted average between the two time distributions characterizing each background component. From these, the centroid positions $C^m_{p|bg}$, $C^m_{bg|p}$, and $C^m_{bg|bg}$ and the numbers of counts $n^m_{p|bg}$, $n^m_{bg|p}$, and $n^m_{bg|bg}$ were obtained. For both delayed and antidelayed time distributions, the *true* centroid position $C^t_{p|p}$ of the time distribution was calculated from the equation

$$C^t_{p|p} = \frac{n^m_{p|p}C^m_{p|p} - n^m_{p|bg}C^m_{p|bg} - n^m_{bg|p}C^m_{bg|p} + n^m_{bg|bg}C^m_{bg|bg}}{n^m_{p|p} - n^m_{p|bg} - n^m_{bg|p} + n^m_{bg|bg}}, \quad (3)$$

where $n^m_{p|p}$ represents the *measured* number of counts of the $p|p$ time distribution. In order to take into account the energy-dependent time walk affecting the centroid position of each background time distribution, these were corrected for the Compton time walk obtained from the Compton curve (see Ref. [32]) before being used in Eq. (3). The measured centroid positions and numbers of counts for each of the eight time components measured and for the final background-corrected delayed and antidelayed time distributions are listed in the first part of Table I. The centroid difference value, ΔC, defined as

$$\Delta C^t = C^{t,\mathrm{del}}_{p|p} - C^{t,\mathrm{antidel}}_{p|p}, \quad (4)$$

was then corrected for the FEP-FEP time walk, which, when the GCD method is used, is usually described by the prompt response difference (PRD) curve. This correction term is given by the value PRD(E_f, E_d), defined as

$$\mathrm{PRD}(E_f, E_d) = \mathrm{PRD}(E_f) - \mathrm{PRD}(E_d). \quad (5)$$

The Compton curve and the PRD curve are shown in Fig. 5. Finally, the lifetime of the level is obtained from the equation

$$\tau = \frac{\Delta C^t - \mathrm{PRD}(E_f, E_d)}{2}. \quad (6)$$

The corrected centroid shift value of $\Delta C^t = 358(19)$ ps, together with a time-walk correction of PRD(520, 333) = 152(6) ps, gave a lifetime for the 2_1^+ level of $\tau = 103(10)$ ps. This is consistent with the literature value of $\tau = 118(20)$ ps, from Ref. [15], and also with the result of $\tau = 116(6)$ ps obtained in Ref. [33], that was never published in a refereed

TABLE I. Centroid positions and number of counts for the $p|p$, $p|bg$, $bg|p$, and $bg|bg$ time distributions, obtained for the lifetime measurements of the 2_1^+, 4_1^+, and 6_1^+ levels in ^{114}Pd. The values are listed for the $p|p$, $p|bg$, $bg|p$, and $bg|bg$ time distributions of both the delayed and antidelayed coincidence peaks. The centroid positions listed for the background time distributions have been corrected for the Compton time walk. For each lifetime measurement, the delayed and antidelayed centroid positions $C^{p|p}$ and the related centroid difference value ΔC are given before and after the background correction from Eq. (3) and labeled with m and t, respectively. The values of the PRD(E_f, E_d) time-walk correction applied in each case are also listed. The lifetime values indicated in bold in the fourth column are the ones measured in this work. At the bottom of the fifth column, for each level, the suggested lifetime value is given (see text for details). All centroid positions, PRD values, and lifetimes are given in picoseconds.

			2_1^+ level in ^{114}Pd		
Delayeds	$C^m_{p\|p}$	$C^m_{p\|bg}$	$C^m_{bg\|p}$	$C^m_{bg\|bg}$	$C^t_{p\|p}$
	130(2)	135(4)	87(4)	98(7)	163(14)
	$n^m_{p\|p}$	$n^m_{p\|bg}$	$n^m_{bg\|p}$	$n^m_{bg\|bg}$	$n^t_{p\|p}$
	15552(125)	7382(72)	8516(98)	5250(91)	4904(196)
Antidel.	$C^m_{p\|p}$	$C^m_{p\|bg}$	$C^m_{bg\|p}$	$C^m_{bg\|bg}$	$C^t_{p\|p}$
	−148(2)	−141(4)	−117(4)	−132(8)	−195(13)
	$n^m_{p\|p}$	$n^m_{p\|bg}$	$n^m_{bg\|p}$	$n^m_{bg\|bg}$	$n^t_{p\|p}$
	16024(127)	7080(69)	8811(100)	4963(86)	5096(195)
	$\Delta C^m = 278(3)$	$\Delta C^t = 358(19)$	PRD = 152(6)	**τ_{meas} = 103(10) → w.a. τ_{2^+} = 113(5)**	
			4_1^+ level in ^{114}Pd		
Delayed	$C^m_{p\|p}$	$C^m_{p\|bg}$	$C^m_{bg\|p}$	$C^m_{bg\|bg}$	$C^t_{p\|p}$
	39(4)	43(5)	32(11)	31(11)	41(21)
	$n^m_{p\|p}$	$n^m_{p\|bg}$	$n^m_{bg\|p}$	$n^m_{bg\|bg}$	$n^t_{p\|p}$
	2797(53)	899(30)	1390(37)	468(22)	976(75)
Antidel.	$C^m_{p\|p}$	$C^m_{p\|bg}$	$C^m_{bg\|p}$	$C^m_{bg\|bg}$	$C^t_{p\|p}$
	−58(4)	−42(5)	−40(11)	−36(11)	−75(15)
	$n^m_{p\|p}$	$n^m_{p\|bg}$	$n^m_{bg\|p}$	$n^m_{bg\|bg}$	$n^t_{p\|p}$
	2825(53)	874(30)	1180(34)	581(24)	1352(74)
	$\Delta C^m = 97(6)$	$\Delta C^t = 116(26)$	PRD = 71(5)	**τ_{meas} = 22(13)**	
			from $\tau_{2^+} + \tau_{4^+}$		
	$\Delta C^m = 411(11)$	$\Delta C^t = 477(38)$	PRD = 231(6)	**τ_{meas} = 20(22)**	**→ w.a. τ_{4^+} = 21(11)**
			6_1^+ level in ^{114}Pd		
Delayed	$C^m_{p\|p}$	$C^m_{p\|bg}$	$C^m_{bg\|p}$	$C^m_{bg\|bg}$	$C^t_{p\|p}$
	7(3)	5(6)	11(5)	19(8)	11(10)
	$n^m_{p\|p}$	$n^m_{p\|bg}$	$n^m_{bg\|p}$	$n^m_{bg\|bg}$	$n^t_{p\|p}$
	3664(61)	1543(39)	1145(34)	639(25)	1616(84)
Antidel.	$C^m_{p\|p}$	$C^m_{p\|bg}$	$C^m_{bg\|p}$	$C^m_{bg\|bg}$	$C^t_{p\|p}$
	−27(4)	−22(5)	−35(6)	−20(9)	−24(11)
	$n^m_{p\|p}$	$n^m_{p\|bg}$	$n^m_{bg\|p}$	$n^m_{bg\|bg}$	$n^t_{p\|p}$
	3512(59)	1522(39)	1011(32)	617(25)	1596(82)
	$\Delta C^m = 34(5)$	$\Delta C^t = 35(15)$	PRD = 30(4)	**τ_{meas} = 2(8) → $\tau_{6^+} \leqslant$ 10**	

journal. The weighted average of the three values is τ_{2^+} = 113(5) ps, and that is the value which will be used later on in the paper.

B. 4_1^+ level in ^{114}Pd

The 4_1^+ level in ^{114}Pd was isolated by applying three background-subtracted HPGe gates on the $2_1^+ \rightarrow 0^+_{g.s.}$, $8_1^+ \rightarrow 6_1^+$, and $10_1^+ \rightarrow 8_1^+$ transitions. The resulting γ-ray spectra are shown in Fig. 6. The energy gates on the $4_1^+ \rightarrow 2_1^+$ and $6_1^+ \rightarrow 4_1^+$ transitions in E_γ(LaBr$_3$(Ce)) are shown by the two pairs of black solid lines. The non-negligible contribution of the 511 keV peak to the peak at 520 keV means that the energy gate on the $4_1^+ \rightarrow 2_1^+$ transition was taken only to the right of the energy peak. The energy gate on the $6_1^+ \rightarrow 4_1^+$ transition was taken as narrow as possible in order to minimize the contributions from the $10_1^+ \rightarrow 8_1^+$ and $7_1^+ \rightarrow 5_1^+$ (659 keV, from the quasi-γ band) transitions. The former is presumably carrying a very short lifetime, from the 10_1^+ level, while the lifetime carried by the latter is unknown. The positions of the two background gates are indicated by the black arrows. For the $4_1^+ \rightarrow 2_1^+$ peak, this was taken as close as possible to the peak. The second background gate was applied around 750 keV of energy, in order to avoid the $3_1^+ \rightarrow 2_1^+$ transition, from the quasi-γ band at 680 keV. Only the background to the right-hand side of the coincidence peak was considered for the *three samples* approach because of the large number of contaminant peaks on the left-hand side of the $6_1^+ \rightarrow 4_1^+$

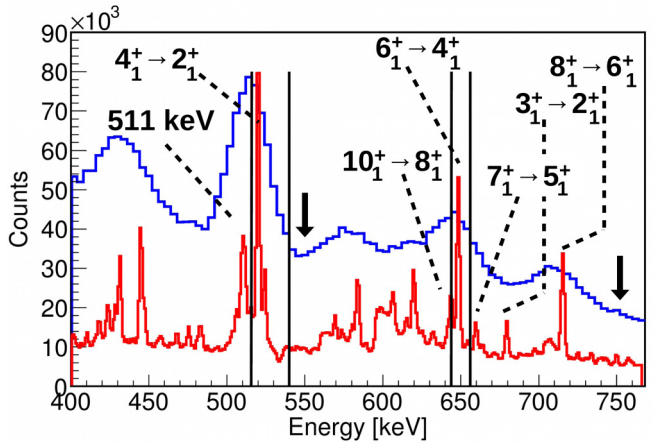

FIG. 6. E_γ(LaBr$_3$(Ce)) (blue) and E_γ(HPGe) (red) spectra obtained in coincidence with the background-subtracted HPGe gates on the $2_1^+ \rightarrow 0_{g.s.}^+$, $8_1^+ \rightarrow 6_1^+$ and $10_1^+ \rightarrow 8_1^+$ transitions. E_γ(LaBr$_3$(Ce)) gates on the $4_1^+ \rightarrow 2_1^+$ and $6_1^+ \rightarrow 4_1^+$ transitions are indicated by the black solid lines. In order to minimize the contributions of contaminant peaks, observable in the E_γ(HPGe) spectrum, these were not centered around the LaBr$_3$(Ce) energy peaks. Background gates for the timing information in the LaBr$_3$(Ce) array are indicated by the black arrows.

transition. At the same time, the asymmetric energy gate for the $6_1^+ \rightarrow 4_1^+$ peak should reduce the contribution from the left-hand-side background significantly. The position of the $p|p$, $p|bg$, $bg|p$, and $bg|bg$ gates are indicated in the projection of the E_γ(LaBr$_3$(Ce))-E_γ(LaBr$_3$(Ce))-ΔT cube in Fig. 7.

A corrected centroid difference value of $\Delta C^t = 116(26)$ ps was found for this measurement (refer to Table I). Combining this value with the time-walk correction of PRD(648, 520) = 71(5) ps, Eq. (6) gives a lifetime of $\tau_{4^+} = 22(13)$ ps.

A second indirect measurement was performed on the lifetime of the 4_1^+ level. E_γ(HPGe) gates were applied on the $8_1^+ \rightarrow 6_1^+$ and $10_1^+ \rightarrow 8_1^+$ transitions, while E_γ(LaBr$_3$(Ce))

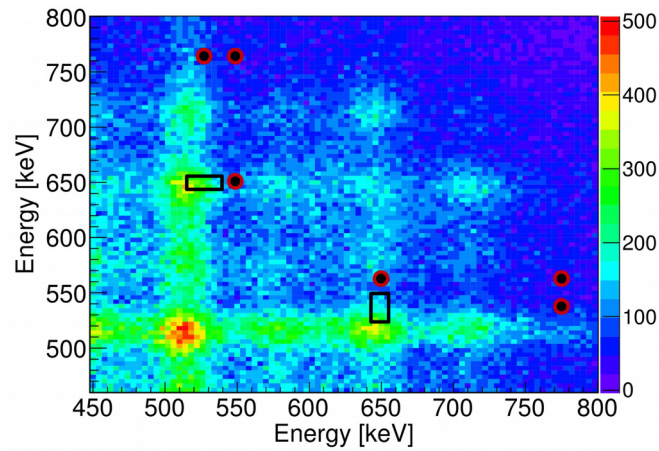

FIG. 7. As in Fig. 4 but gated on the background-subtracted $2_1^+ \rightarrow 0_{g.s.}^+$, $8_1^+ \rightarrow 6_1^+$, and $10_1^+ \rightarrow 8_1^+$ transitions, in Gammasphere. The black solid lines define the limits of the gates applied on the delayed and antidelayed coincidence peaks, while the black dots represent the three background samples selected for each peak.

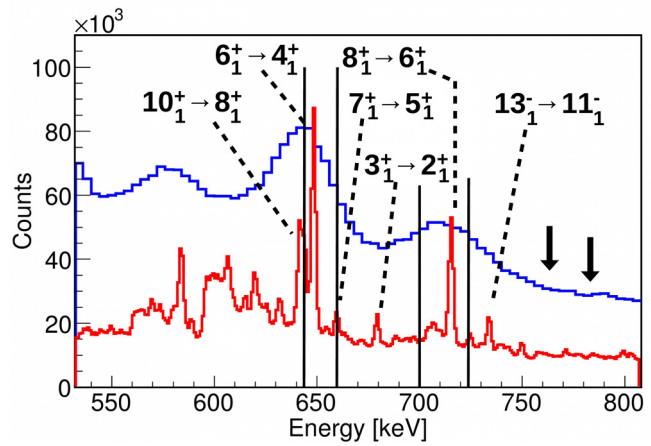

FIG. 8. E_γ(LaBr$_3$) (blue) and E_γ(HPGe) (red) spectra obtained from the two background-subtracted HPGe gates on the $2_1^+ \rightarrow 0_{g.s.}^+$ and $4_1^+ \rightarrow 2_1^+$ transitions. Energy gates on the feeding and depopulating transitions are indicated by the black solid lines. Background gates for the timing information on the LaBr$_3$ array are indicated by the two black arrows.

start and stop gates were applied on the $2_1^+ \rightarrow 0_{g.s.}^+$ and $6_1^+ \rightarrow 4_1^+$ transitions. A background-corrected centroid difference value of $\Delta C = 477(38)$ ps was obtained and, by using the time-walk correction PRD(648, 333) = 231(6) ps, the lifetime $\tau_{2^+} + \tau_{4^+} = 123(19)$ ps was measured. The lifetime of $\tau_{2^+} = 103(10)$ ps was subtracted from this sum of two lifetimes, and the value $\tau_{4^+} = 20(22)$ ps was obtained. The weighted average between the two lifetime measurements (direct and indirect) for the 4_1^+ level gives $\tau_{4^+} = 21(11)$ ps.

C. 6_1^+ level in ^{114}Pd

The lifetime of the 6_1^+ level in ^{114}Pd was determined after gating on the background-subtracted $2_1^+ \rightarrow 0_{g.s.}^+$ and $4_1^+ \rightarrow 2_1^+$ transitions in Gammasphere. E_γ(LaBr$_3$(Ce)) (blue) and E_γ(HPGe) (red) spectra are shown in Fig. 8. As for the case of the 4_1^+ level, in order to minimize the contribution from the $10_1^+ \rightarrow 8_1^+$ transition, the E_γ(LaBr$_3$(Ce)) gate on the $6_1^+ \rightarrow 4_1^+$ transition was set asymmetrically to the right-hand side of the peak. Any background gate taken to the immediate right of the 648 keV peak, or to the left of the 715 keV peak, would include also events from the $3_1^+ \rightarrow 2_1^+$ transition, and therefore the background gate for the $6_1^+ \rightarrow 4_1^+$ transition was set around $E_\gamma = 760$ keV. As for the previous case, many peaks can be observed to the left of the $6_1^+ \rightarrow 4_1^+$ transition, and for this reason a left background gate was excluded also for this peak. The background gate for the $8_1^+ \rightarrow 6_1^+$ transition was applied around $E_\gamma = 780$ keV. The positions of the two FEP and the background gates are indicated in Fig. 8 by the two black arrows and by the black dots in the two-dimensional projection of the E_γ-E_γ-ΔT cube, shown in Fig. 9. The measured centroid positions and numbers of counts for the eight time distributions considered for this measurement are listed in the bottom part of Table I. A corrected centroid difference value of $\Delta C^t = 35(15)$ ps was found. Combined with a time-walk correction of PRD(715, 648) = 30(4) ps, the lifetime

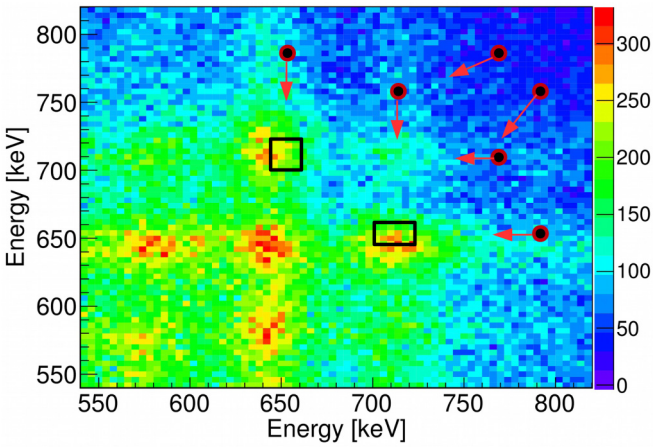

FIG. 9. As in Fig. 4, but obtained by gating on the background-subtracted $2_1^+ \rightarrow 0_{g.s.}^+$ and $4_1^+ \rightarrow 2_1^+$ transitions in Gammasphere. The background regions are indicated by the black dots and the red arrows indicate to which of the two coincidence peaks they refer.

value obtained was $\tau_{6^+} = 2(8)$ ps. This was translated into an upper limit for this lifetime of 10 ps.

IV. INTERPRETATION OF RESULTS

The Weisskopf hindrance factor F_W is defined as

$$F_W = \frac{\tau_\gamma}{\tau_W}, \tag{7}$$

where τ_W is the single-particle Weisskopf estimate of the lifetime and τ_γ is the partial lifetime defined as

$$\tau_\gamma = \tau_{\text{meas}}(1+\alpha), \tag{8}$$

where α is the electron conversion coefficient taken from BRIcc [34]. For each of the three measured lifetimes F_W is in the order of magnitude of 10^{-2}, which indicates a collective behavior for the excited levels in the yrast band of ^{114}Pd.

The $B(E2)$ transition strengths in e^2b^2 units were calculated using the equation

$$B(E2; J_i \rightarrow J_i - 2) = \frac{8.162 \times 10^{10}}{\tau_\gamma E_\gamma^5}, \tag{9}$$

where τ_γ is in nanoseconds and the energy E_γ of the transition is in keV. The uncertainties $\sigma_{B(E2)}$ are assumed to be symmetric, and were estimated following the procedure given in Ref. [35]. This is usually recommended when the uncertainties associated to the lifetime measurements are either asymmetric or exceed 10%. Intrinsic quadrupole moments Q_0 for the levels of interest were calculated using the relationship between $B(E2; J \rightarrow J-2)$ and Q_0, described by the equation

$$B(E2; J_i \rightarrow J_f) = \frac{5}{16\pi} e^2 Q_0^2 \langle J_i K 20 | J_f K \rangle^2, \tag{10}$$

where the expression in brackets $\langle \cdots \rangle$ is the Clebsch-Gordon coefficient. Uncertainties on Q_0 were obtained by propagating the uncertainties on $B(E2)$. Deformation parameters $|\beta_2|$ for each level were calculated solving the cubic equation [1]

$$Q_0 = \frac{3}{\sqrt{5\pi}} R_{av}^2 Z \beta_2 \left(1 + \frac{2}{7}\sqrt{\frac{5}{\pi}}\beta_2 + \frac{1}{14\pi}\beta_2^2 + \cdots\right), \tag{11}$$

valid in the assumption of a quadrupoloid shape. The value of $R_{av} = 1.2A^{1/3}$ fm was used. Uncertainties for the different $|\beta_2|$ values were obtained by solving the same equation for the upper and lower limits of Q_0. Partial level lifetimes τ_γ, reduced transition probabilities $B(E2)$, intrinsic quadrupole moments Q_0, and deformation parameters $|\beta_2|$ for the 2_1^+, 4_1^+, and 6_1^+ levels in ^{114}Pd are listed in Table. II.

TABLE II. Partial lifetimes τ_γ, reduced transition probabilities $B(E2 : J_i \rightarrow J_i - 2)$, together with intrinsic quadrupole moments Q_0 and deformation parameters $|\beta_2|$ for ^{114}Pd. One W.u. equals $32.84 \times 10^{-4}\ e^2b^2$.

	τ_γ	$B(E2; J_i \rightarrow J_i - 2)$		$\lvert Q_0 \rvert$	
J_i^π	(ps)	(e^2b^2)	(W.u.)	(eb)	$\lvert\beta_2\rvert$
2_1^+	115(5)	0.174(7)	53(2)	2.96(6)	0.231(5)
4_1^+	21(11)	0.140(73)	43(27)	2.22(58)	0.177(44)
6_1^+	$\leqslant$10	$\geqslant$0.071	$\geqslant$21	$\geqslant$1.51	$\geqslant$0.123

In the Davydov-Filippov model [17] for rigid triaxial rotors, $B(E2)$ values between the ground-state band and quasi-γ band are able to provide a signature of triaxiality; however, as shown in Ref. [36], for values of γ going from 0° to 60°, $B(E2)$ values for transitions between levels inside the ground-state band change by less than 10%, which is below the experimental uncertainties on the $B(E2)$ values presented in this work.

Figure 10 shows the comparison between measured $B(E2)$ values (black dots) and theoretical values from the projected shell model (PSM) [14] (squares) and using the Bohr Hamiltonian coupled with the Killingbeck potential [20] (triangles,

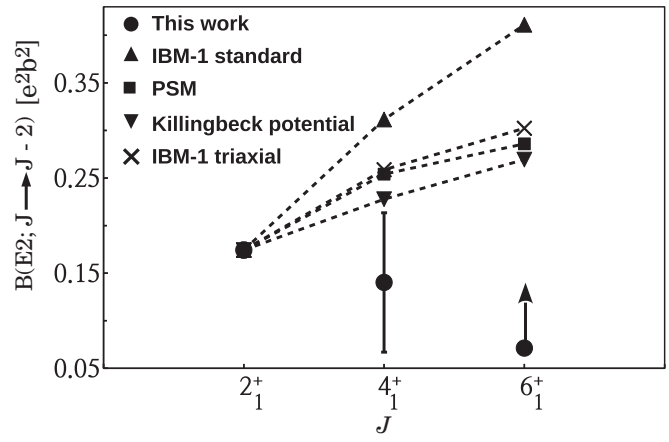

FIG. 10. Theoretical values of the reduced transition probabilities for the $2_1^+ \rightarrow 0_{g.s.}^+$, $4_1^+ \rightarrow 2_1^+$, and $6_1^+ \rightarrow 4_1^+$ transitions in ^{114}Pd, obtained from PSM (squares) [14], Killingbeck potential (triangles, down) [20], standard IBM-1 (triangles, up), and triaxial IBM-1 (crosses) [37], compared with experimental values (black dots).

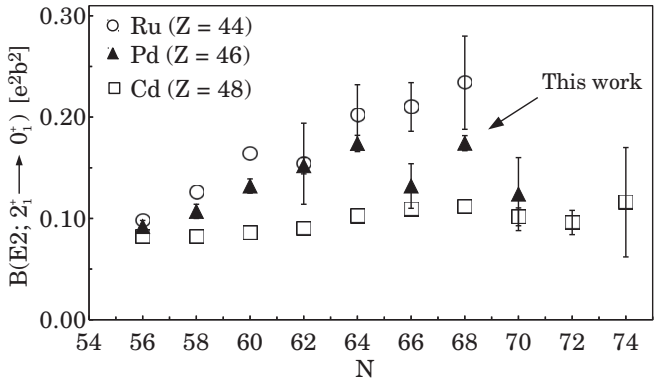

FIG. 11. $B(E2; 2_1^+ \rightarrow 0_{g.s.}^+)$ transition rates for the Ru ($Z = 44$, circles), Pd ($Z = 46$, triangles), and Cd ($Z = 48$, squares) isotopic chains. Values are taken from Ref. [35], except for ^{114}Pd ($N = 68$) which corresponds to $\tau_{2^+} = 113(5)$ ps. Error bars are not shown when they are smaller than the data points.

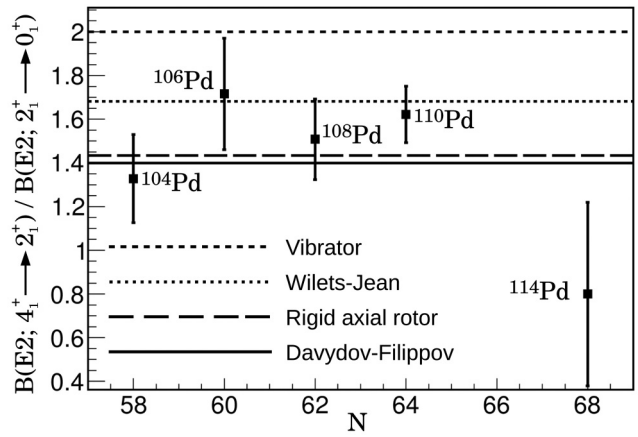

FIG. 12. Experimental $R_{B(E2)}$ values for ^{104,106,108,110}Pd, taken from Ref. [27], and for ^{114}Pd measured in this work. The ratios are compared with the values predicted by the vibrator, rigid axial rotor, Wilets-Jean and Davydov-Filippov models, as indicated in the legend.

down). In this last work ^{114}Pd was assumed to be triaxial. In the IBM-1 calculations in Ref. [37] two different approaches were used to calculate $B(E2)$ transition rates in ^{114}Pd. An SU(3)-type Hamiltonian was used first (triangles, up), and then a three-body term (three d bosons) able to create a triaxial minimum in the potential was added (crosses). The effect of this additional interaction is to strongly modify the distribution of the energy levels belonging to the γ band, reducing the odd-even staggering $S(J)$ described previously [38]. As pointed out in Ref. [37], the three-body term reduces the relative $B(E2)$ values for the ground-state band, by a factor of $\approx$0.8, leading to a better agreement with the experimental $B(E2)$ values as shown in Fig. 10. IBM-2 calculations [39] (not in the figure) give a relative $B(E2; 4_1^+ \rightarrow 2_1^+)$ value of 0.25 e^2b^2 which overlaps with those from PSM and the triaxial IBM-1 [the $B(E2; 6_1^+ \rightarrow 4_1^+)$ value was not calculated in this model]. All calculations were normalized to the $B(E2; 2_1^+ \rightarrow 0_1^+)$ value measured in this work.

Figure 10 shows that none of the calculations for the $B(E2; 4_1^+ \rightarrow 2_1^+)$ value are within one standard deviation of the experimental value; the closest is for the Killingbeck potential, which is at 1.2 standard deviations. This calculation explicitly includes the triaxial deformation, and this may be why it shows better agreement. Indeed, the $B(E2; 4_1^+ \rightarrow 2_1^+)$ values calculated in the two versions of the IBM-1 show the importance of triaxiality. However, in order to get a better understanding, it would be necessary to measure the lifetimes of the first excited states of the quasi-γ band, which is not possible with this data set.

Additional information can be obtained by analyzing the systematics of the $B(E2; 2_1^+ \rightarrow 0_1^+)$ values for the neighboring even-Z isotopic chains, i.e., Cd and Ru, as shown in Fig. 11. Even-even cadmium isotopes in the range $N = 56$–72 are considered to be good examples of spherical anharmonic vibrators [9,40,41], while among the even-even Ru isotopes cases of γ softness and stable triaxiality in the range $^{100-118}$Ru were observed [6,7]. Figure 11 shows that, as the number of neutrons N increases, the Ru and Cd isotopic chains follow completely different paths. The $B(E2)$ values for the cadmium chain are rather constant while Ru transition rates increase up to a maximum value for ^{112}Ru, where the maximum of triaxiality is expected to occur [6]. The $B(E2)$ values for the Pd chain lie in between those of Cd and Ru for almost every value of N, but it is interesting that the adopted value of ^{114}Pd approaches that of ^{112}Ru, indicating some degree of triaxiality. Moreover, Q_0 values in the ground-state band of molybdenum and ruthenium, which are associated with γ deformation, were observed to decrease for increasing J values [4], and this is consistent with the values quoted in Table II for the 2^+ and 4^+ levels in ^{114}Pd.

Figure 11 also hints at some sort of staggering behavior between ^{112}Pd and ^{116}Pd. However, the lifetime measurements of the first 2^+ levels in ^{112}Pd and ^{116}Pd were performed using the recoil distance method in Refs. [42] and [43], respectively. In both works, the palladium isotopes were observed following the spontaneous fission of ^{252}Cf, and γ rays were detected in singles, in coincidence with fission fragments. Considering that lifetimes were obtained by measuring the absolute or relative intensities of the $2_1^+ \rightarrow 0_1^+$ transition in the two nuclei and that high-J levels are likely to be populated, it is possible that some feeding transitions contribute to the lifetimes measured in the two experiments. The lifetime measured would then be larger than that for the 2_1^+ level, leading to correspondingly smaller $B(E2; 2_1^+ \rightarrow 0_1^+)$ values.

The ratio $R_{B(E2)} = B(E2; 4_1^+ \rightarrow 2_1^+)/B(E2; 2_1^+ \rightarrow 0_1^+)$ is indicative of the degree of collectivity: $R_{B(E2)} = 2$ for vibrational nuclei [25], 1.43 for rigid axial nuclei [44], 1.68 for γ-unstable rotors [45], and 1.40 for rigid triaxial rotors [46], in the case of $\gamma = 27.5^\circ$. The $B(E2; J_i \rightarrow J_i - 2)$ values in Table II give a value of $R_{B(E2)} = 0.80(42)$ for ^{114}Pd, and this is compared with the experimental ratios measured in Coulomb excitation experiments for ^{104,106,108,110}Pd in Fig. 12. It can be observed that the $R_{B(E2)}$ values of Pd isotopes for $N = 60, 62, 64$ fluctuate around the limit of 1.68 given by the Wilets-Jean model, although the value for ^{104}Pd ($N = 58$) is slightly smaller. A sudden drop of the $R_{B(E2)}$ value is observed

for $N = 68$, and, while the experimental value is more than 1 standard deviation from the value for either rigid axial or triaxial deformation, it is consistent within 1.4σ with the conclusion suggested by the energy staggering $S(J)$, shown in Fig. 1, that there is an inversion to rigid triaxial behavior at ^{114}Pd.

V. CONCLUSIONS

This work reports on the first measurements of lifetimes of excited levels in fission fragments using the large-scale array Gammasphere + FATIMA. The hybrid array, at the Argonne National Laboratory, used 51 HPGe detectors coupled to 25 $LaBr_3$(Ce) scintillators. A fully digital acquisition setup was used for the first time.

A lifetime measurement of the 2_1^+ level in ^{114}Pd gave a value of $\tau_{2^+} = 103(10)$ ps, which was found to be consistent with previous measurements [15,33]. Values of $\tau_{4^+} = 22(13)$ ps and $\tau_{6^+} \leqslant 10$ ps were also obtained. From the lifetimes measured, $B(E2)$ transition strengths and quadrupole moments Q_0 were calculated, along with their associated deformation parameters $|\beta_2|$. None of the theoretical calculations performed using the IBM [37–39], PSM [14], and collective model calculations [20] are within 1σ of the measured $B(E2; 4_1^+ \rightarrow 2_1^+)$ value, but the closest is the one obtained from the Killingbeck potential, probably because of the inclusion of a triaxial minimum. The lower limit obtained for the $B(E2; 6_1^+ \rightarrow 4_1^+)$ value is in agreement with all the calculations.

The suggestion that ^{114}Pd is one of the most deformed of all Pd isotopes is strongly supported by the $B(E2; 2_1^+ \rightarrow 0_1^+)$ value, which is one of the largest of the isotopic chain. The systematics of the $B(E2)$ values for even-even palladium isotopes compared with the ones of the even-even neighboring ruthenium and cadmium isotopes shows an onset of triaxiality that reaches a maximum for ^{114}Pd.

The experimental $R_{B(E2)}$ ratio was compared with the expectations from different models and a transition from γ-soft rotor to that of a rigid triaxially deformed configuration seems to be taking place for $N = 68$.

Any measurement of interband $B(E2)$ values was precluded by the lack of statistics, with $LaBr_3$(Ce) detectors, for the transitions between the quasi-γ and ground-state bands. This forbids any quantitative evaluation of the triaxial deformation characterizing ^{114}Pd, and therefore new data will be necessary to draw any definitive conclusion.

ACKNOWLEDGMENTS

This work was financially supported by the Science and Technology Facility Council (STFC) Grants No. ST/L005840/1, No. ST/L005743/1, and No. ST/G000751/1. This work has also been partially supported by the U.S. Department of Energy, Office of Science, Office of Nuclear Physics under Contract No. DE-AC02-06CH11357 (ANL). E.R.G. would like to acknowledge the STFC for funding via his Ph.D. studentship. D.J.H. acknowledges the National Science Foundation, Grant No. PHY-1502092. E.A.S. and O.Y. would like to acknowledge the project DFNI-E02/6. This research used resources of the Argonne National Laboratory ATLAS facility, which is a DOE Office of Science User Facility.

[1] K. E. G. Lobner, M. Vetter, and V. Hönig, Nucl. Data Tables **7**, 495 (1970).
[2] A. Bohr, Dan. Mat. Fys. Medd. **26**, 14 (1952).
[3] H. Watanabe *et al.*, Phys. Lett. B **704**, 270 (2011).
[4] J. B. Snyder *et al.*, Phys. Lett. B **723**, 61 (2013).
[5] Y. X. Luo *et al.*, Phys. Lett. B **670**, 307 (2009).
[6] D. T. Doherty *et al.*, Phys. Lett. B **766**, 334 (2017).
[7] P.–A. Söderström *et al.*, Phys. Rev. C **88**, 024301 (2013).
[8] S. Lalkovski *et al.*, Eur. Phys. J. A **18**, 589 (2003).
[9] Y. X. Luo *et al.*, Nucl. Phys. A **874**, 32 (2012).
[10] L. E. Svensson *et al.*, Nucl. Phys. A **584**, 547 (1995).
[11] Y. Wang *et al.*, Phys. Rev. C **63**, 024309 (2001).
[12] X. Q. Zhang, J. H. Hamilton, A. V. Ramayya, S. J. Zhu, J. K. Hwang, C. J. Beyer, J. Kormicki, E. F. Jones, P. M. Gore *et al.*, Phys. Rev. C **63**, 027302 (2001).
[13] M. A. Stoyer *et al.*, Nucl. Phys. A **787**, 455 (2007).
[14] R. Chaudhary *et al.*, Eur. Phys. J Plus **133**, 81 (2018).
[15] A. Dewald, K. Starosta, P. Petkov, M. Hackstein, W. Rother, P. Adrich, A. M. Amthor, T. Baumann, D. Bazin *et al.*, Phys. Rev. C **78**, 051302(R) (2008).
[16] L. Wilets and M. Jean, Phys. Rev. **102**, 788 (1956).
[17] A. S. Davydov and G. F. Filippov, Sov. Phys. JETP **6**, 33 (1958).
[18] N. V. Zamfir and R. F. Casten, Phys. Lett. B **260**, 265 (1991).
[19] S. Frauendorf, Int. J. Mod. Phys. **24**, 1541001 (2015).
[20] H. Sobhani *et al.*, Nucl. Phys. A **973**, 33 (2018).
[21] A. C. Wahl, in *Symposium on Physics and Chemistry of Fission*, Salzburg, 22–26 March 1965 (IAEA, Vienna, 1965).
[22] A. Arima and F. Iachello, Phys. Rev. Lett. **35**, 1069 (1975).
[23] F. Iachello and A. Arima, *The Interacting Boson Model* (Cambridge University Press, Cambridge, 1987).
[24] K. Hara and Y. Sun, Int. J. Mod. Phys. **4**, 637 (1995).
[25] A. Bohr and B. R. Mottelson, *Nuclear Structure* (World Scientific, Singapore, 1975), Vols. 1 and 2.
[26] J. Killingbeck, J. Phys. A: Math. Gen. **13**, L393 (1980).
[27] https://www.nndc.bnl.gov
[28] I.-Y. Lee *et al.*, Nucl. Phys. A **520**, c641 (1990).
[29] O. J. Roberts *et al.*, Nucl. Instrum. Methods Phys. Res. Sect. A **748**, 91 (2014).
[30] M. Rudigier *et al.*, Acta Phys. Pol. B **48**, 351 (2017).
[31] J.-M Régis *et al.*, Nucl. Instrum. Methods Phys. Res. Sect. A **726**, 191 (2013).
[32] E. R. Gamba, A. M. Bruce, and M. Rudigier, Nucl. Instrum. Methods Phys. Res. Sect. A **928**, 93 (2019).
[33] H. Mach *et al.*, *JYFL annual report* (University of Jyväskylä, Jyväskylä, Finland, 2003).
[34] http://bricc.anu.edu.au
[35] S. Raman, C. J. Nestor, and P. Tikkanen, At. Data Nucl. Data Tables **78**, 1 (2001).
[36] H. Toki and A. Faessler, Z. Phys. A **276**, 35 (1976).

[37] B. Sorgunlu and P. Van Isacker, Nucl. Phys. A **808**, 27 (2008).
[38] P. Van Isacker (private communication).
[39] K.-H. Kim *et al.*, Nucl. Phys. A **604**, 163 (1996).
[40] A. Jokinen *et al.*, in *Proceedings of the Third International Conference on Fission and Properties of Neutron-Rich Nuclei*, Sanibel Island, FL,2002 (World Scientific, Singapore, 2003).
[41] A. Aprahamian *et al.*, Phys. Lett. B **140**, 22 (1984).
[42] G. Mamane *et al.*, Nucl. Phys. A **454**, 213 (1986).
[43] R. C. Jared, H. Nifenecker, and S. G. Thompson, presented at the Third Symposium on the Physics and Chemistry of Fission, Rochester, NY, 1973 (unpublished).
[44] G. Alaga, K. Aider, A. Bohr, and B. Mottelson, Dan. Mat. Fys. Medd. **29**, 9 (1955).
[45] F. Iachello, Phys. Rev. Lett. **85**, 3580 (2000).
[46] A. S. Davydov and V. S. Rostovski, Nucl. Phys. **12**, 58 (1959).